Materials Today Bio 28 (2024) 101193

Contents lists available at ScienceDirect

Materials Today Bio

journal homepage: www.journals.elsevier.com/materials-today-bio

Silk films with distinct surface topography modulate plasma membrane curvature to polarize macrophages

Doudou Hu [a,b], Tiandong Li [a,b], Haixu Bian [a], Haiyu Liu [a], Pengwei Wang [a], Yeyuan Wang [a], Jingchen Sun [a,*]

[a] Subtropical Sericulture and Mulberry Resources Protection and Safety Engineering Research Center, College of Animal Science, South China Agricultural University, Guangzhou, Guangdong, 510642, China

[b] State Key Laboratory of Quality Research in Chinese Medicine, Institute of Chinese Medical Sciences, University of Macau, Taipa, Macau SAR, 999078, China

ARTICLE INFO

Keywords:
Silk fibroin
Film
Macrophage
Polarization
Surface topology

ABSTRACT

The physical properties of a biomaterial play a vital role in modulating macrophage polarization. However, discerning the specific effects of individual parameters can be intricate due to their interdependencies, limiting the mechanism underlying a specific parameter on the polarization of macrophages. Here, we engineered silk fibroin (SF) films with tunable surface roughness while maintaining similar physical properties by combining casting and salting out techniques. We demonstrate that increased surface roughness in SF films promotes M2-like macrophage polarization, characterized by enhanced secretion of anti-inflammatory cytokines. Transcriptomic analysis unveils the modulation of genes associated with extracellular matrix-cell interactions, highlighting the role of surface topography in regulating cellular processes. Mechanistically, we show that surface roughness induces macrophage membrane curvature, facilitating integrin αv endocytosis and thereby inhibiting the integrin-NF-kB signaling pathway. In vivo implantation assays corroborate that rough SF films substantially mitigate early inflammatory responses. This work establishes a direct link between surface roughness and intracellular signaling in macrophages, adding to our understanding of the biomaterial surface effect at the material-cell interface and bringing insights into material design.

1. Introduction

Macrophages play a crucial role in tissue injury and repair, exerting significant influence on wound healing dynamics [1]. These immune cells possess remarkable plasticity, enabling them to dynamically respond and adapt to diverse physiological and pathological tissue microenvironments. Typically, macrophages can transition between pro-inflammatory (M1) and anti-inflammatory (M2) phenotypes in response to various microenvironmental cues [2].

In the last decade, biomaterial properties have been recognized as important modulators of macrophage response and subsequent tissue regeneration. A body of studies has highlighted surface topography, wettability, substrate stiffness, and material components as key factors influencing macrophage polarization [3–6]. Regarding surface topography, roughness is one of the typical physical properties of biomaterials. Numerous investigations have been conducted to explore the impact of surface roughness on macrophage polarization. However, several challenges persist in this area.

Firstly, no consensus has been reached on this issue. While the majority of studies support the notion that hydrophilic and rough surfaces induce anti-inflammatory macrophages [7–15], some hold divergent perspectives [16–19], and some report no direct relationship [20]. One plausible explanation for this inconsistency lies in the inherent interdependence of various material properties. Altering one parameter of a biomaterial often results in concomitant changes in other properties, complicating the investigation of the specific effects of individual factors. For example, modifications in surface topography often influence other physicochemical properties of a biomaterial, such as wettability, porosity, stiffness, composition, *etc* [13,14,16,21–23].

Secondly, the mechanism of surface roughness on macrophage polarization remains elusive. Although some insights have been shed on this issue, including the involvement of Wnt signaling [24,25]. autophagy pathway [11], oxidative stress regulation [26], and FAK-MAPK signaling [27], direct evidence linking surface properties and macrophage phenotype is still lacking. For instance, titanium surfaces with varying roughness and hydrophobicity have been shown to regulate

* Corresponding author.
E-mail address: cyfz@scau.edu.cn (J. Sun).

https://doi.org/10.1016/j.mtbio.2024.101193
Received 26 March 2024; Received in revised form 3 August 2024; Accepted 6 August 2024
Available online 8 August 2024

macrophage polarization via Wnt signaling [24,25]. However, the specific mechanism by which surface roughness activates this signaling pathway is unknown. Currently, a gap exists between biomaterial surface properties and the intracellular events governing macrophage polarization. Therefore, it is imperative to uncover direct insights into how the surface roughness of a biomaterial triggers macrophage polarization pathways.

Silk fibroin (SF), a natural protein derived from the silkworm *Bombyx mori,* is a promising biopolymer widely explored in tissue engineering and drug delivery [28,29]. Early comparative studies have revealed that SF-based biomaterials elicited weaker inflammatory responses than other natural and synthetic materials [30,31], showing their good biocompatibility. Moreover, it has been reported recently that SF itself and its degradation products can polarize pro-inflammatory macrophages into an anti-inflammatory phenotype [32]. Nevertheless, when fabricated into a biomaterial, the immune response of SF-based biomaterials not only depends on SF itself but also the physical [22,33] and chemical [34,35] properties of these biomaterials. In this study, to address the mechanism underlying surface roughness on macrophage behaviors, we fabricated SF films with tunable roughness while maintaining similar physical properties. We assessed macrophage polarization on different SF films and explored the underlying mechanisms. It was shown that SF films with varying degrees of roughness were prepared by the combination of casting and salting out techniques. SF film with high roughness promoted M2-like macrophages whereas low roughness favored M1-like macrophages. Furthermore, we identified the expression differences of integrin αv and its downstream signaling pathways between macrophages cultured on the two SF films. Meanwhile, we observed that the surface roughness of SF films influenced the plasma membrane curvature of macrophages, thereby modulating the endocytosis of integrin αv (Scheme 1).

2. Results

2.1. Surface roughness varies among SF films with similar physical parameters

SF films with different surface roughness were prepared by casting and post-treatment. Initially, we obtained two SF films by modulating the drying time of the casting SF solutions. Compared with traditional SF films prepared by fast air-drying (termed as PF film), the one prepared by slow drying method (PS film) had a totally different surface morphology. The PF film was visually transparent whereas the PS film was translucent (Fig. S1). Then, we used ammonium sulfate or methanol to separately soak the two SF films, yielding salt-treated films (YF and YS films), and methanol-treated ones (MF and MS films). The surface morphology of the six SF films was observed by scanning electron microscope (SEM) (Fig. 1a, Fig. S2). The surface of the PF film was flat with barely observable structures, even at a high magnification. Conversely, the surface of PS film showed an irregular fluctuation at a submicrometer scale. Following salting out or methanol treatment, the morphology of the resulting SF films differed in nuance. Furthermore, the surface topography of SF films obtained by different techniques was characterized by atomic force microscopical (AFM). Markedly, slow air-drying induced SF films to transform from a flat surface to a rough surface. Salting out decreased the roughness of the YS film while methanol led to an MS film with a high roughness (Fig. 1b). The surface roughness of the SF films was quantified by three different roughness values including root-mean-square height data (Rq), mean roughness (Ra), and Z-range (Fig. 1c–e). All three roughness values displayed the same trend, with the smallest roughness values for the PF film and the highest roughness for the PS film, respectively. Salting out and methanol treatment can differentially change the roughness of SF films.

The wettability of SF films was shown in Fig. 2a and b. Except that the water contact angle value of the PF film was about 30°, the values of the rest of the SF films were increased from 41° to 68°. Nevertheless, all of the SF films can be considered to be hydrophilic as the contact angle values are below 90°. We next investigated the water insolubility of the SF films. Soaking the PF film in phosphate-buffered saline (PBS) for 24 h resulted in about 20 % weight loss, while 4.3–9.3 % weight loss was observed in the rest of the SF films (Fig. 2c). It suggests that fast-dried PF film can hardly maintain its morphology in physiological fluids. In contrast, slowly-dried PS film and post-treated films were enabled to resist dissolution. Then, the mechanical properties of SF films were determined in wet conditions (Fig. 2d–f). In terms of tensile modulus, the films of PS, YF, and YS were similar, the modulus of which was lower than methanol-treated films. To explore the structural changes by different treatments, FTIR spectra were collected from the SF films (Fig. 2g). It showed that the amide I band of PF film was centered around 1658 cm^{-1}, indicating the characteristic of random coil and α-helices. In

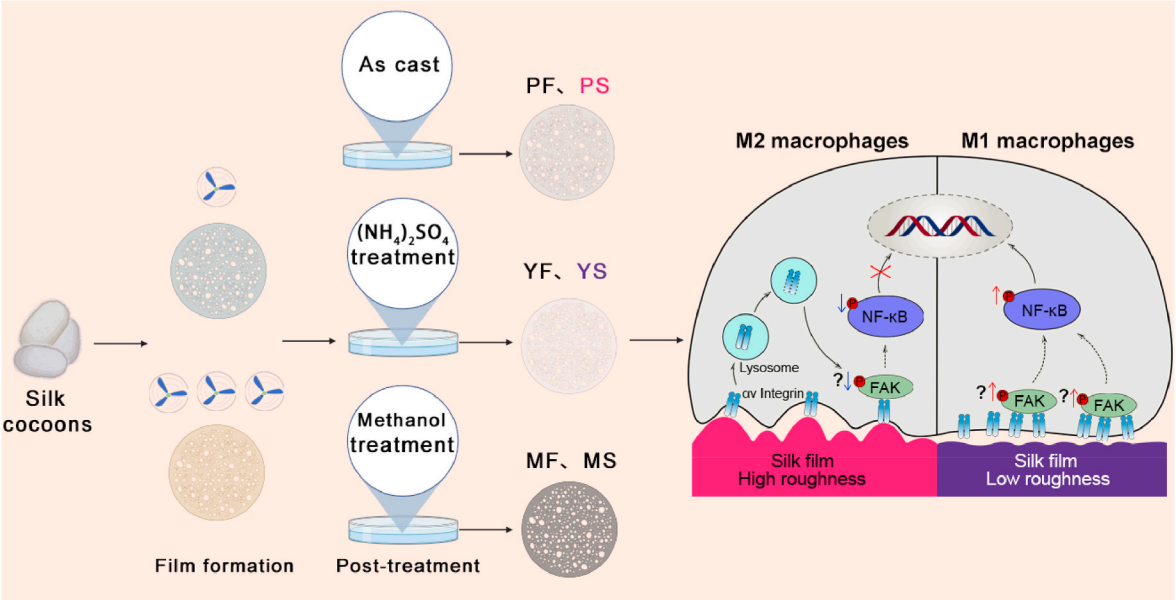

Scheme 1. Preparation and screening of SF films with different surface roughness and the potential mechanism of roughness on macrophage polarization. Part of the scheme is created by BioRender.

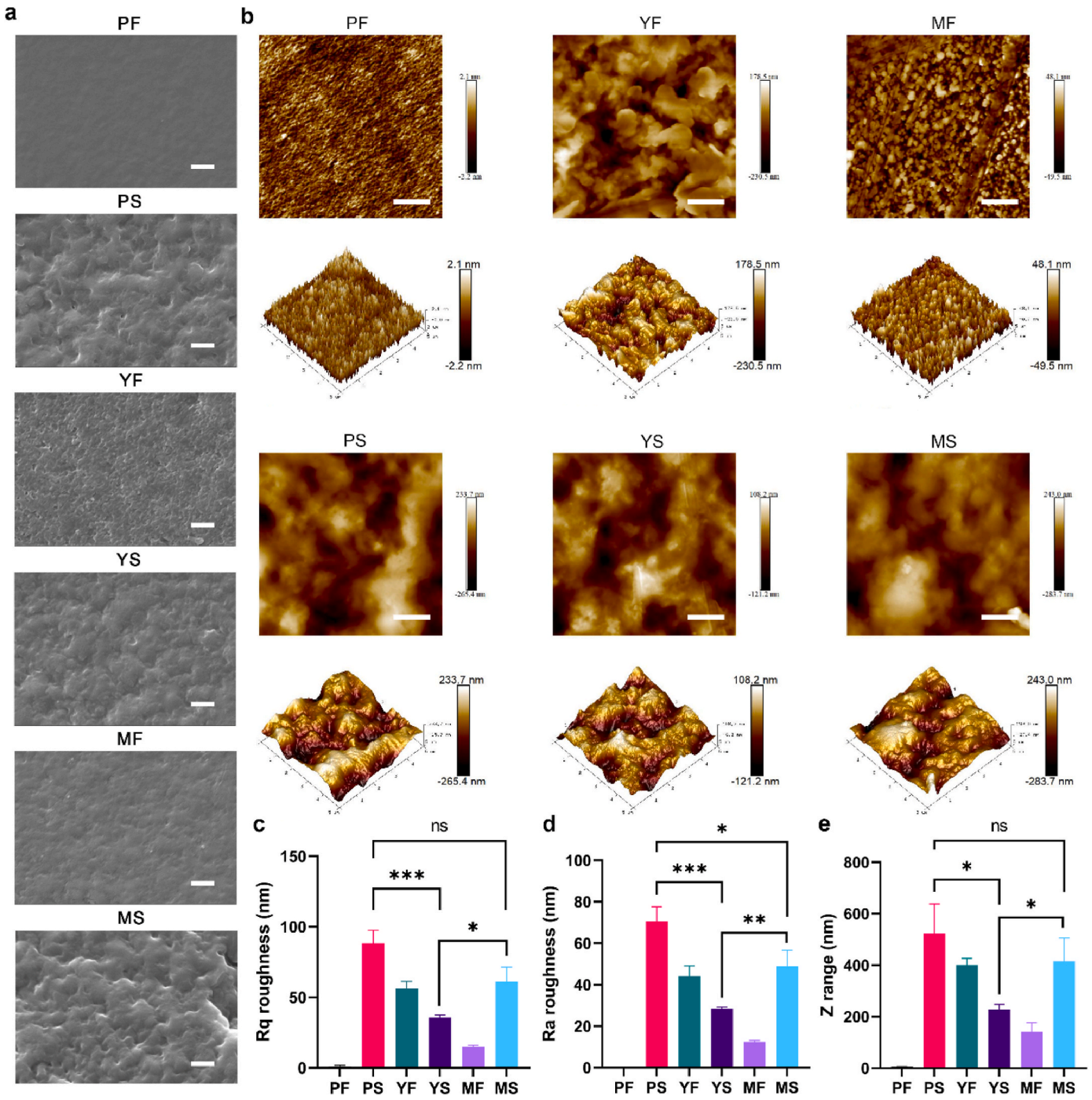

Fig. 1. The surface roughness of the SF films can be tuned. (a) Scanning electron microscope (SEM) images of SF films in a dry state. Scale bar, 1 μm. (b) Atomic force microscopical (AFM) images of the SF films. Scale bar, 1 μm. (c–e) Roughness values (Rq (c), Ra (d), and Z range (e)) of the SF films. Data are expressed as mean ± SD (n = 3). $^{*}p < 0.05$, $^{**}p < 0.01$, $^{***}p < 0.001$, one-way ANOVA with Tukey post-hoc test. ns, not significant. PF: as cast fast drying film, PS: as cast slow drying film, YF: salting out-treated fast drying film, YS: salting out-treated slow drying film, MF: methanol-soaked fast drying film, MS: methanol-soaked slow drying film.

contrast, the peak of the amide I band of PS was shifted to around 1637 cm^{-1}, corresponding to β-sheets. It implied that compared with fast drying, slow drying casting enabled a conformation transition of SF from α-helices to β-sheets. To further characterize the secondary structure of SF films, the amide I band was deconvoluted to determine the fraction of the β-sheets. The relative ratios of different secondary structures of the SF films were estimated from the amide I region (Fig. 2h, S3). PS, YF, YS, and MF films all experienced a transition from α-helices to β-sheets, indicating the transition from an amorphous state to a crystallite. These data show that the wettability and mechanical properties of PS, YF, and YS films kept similar following different treatments. Together, the surface roughness of the three SF films can be decoupled from other physical features following casting and salting out.

2.2. SF films with tunable roughness differentially polarize macrophages

Cellular viability of two cell lines (RAW 264.7 and L929) on SF films was first investigated. Compared with the tissue culture plate (TCP), no significant differences in cell viability were observed on all five SF films, no matter for RAW 264.7 (Fig. S4a) and L929 cells (Fig. S4b). It indicates

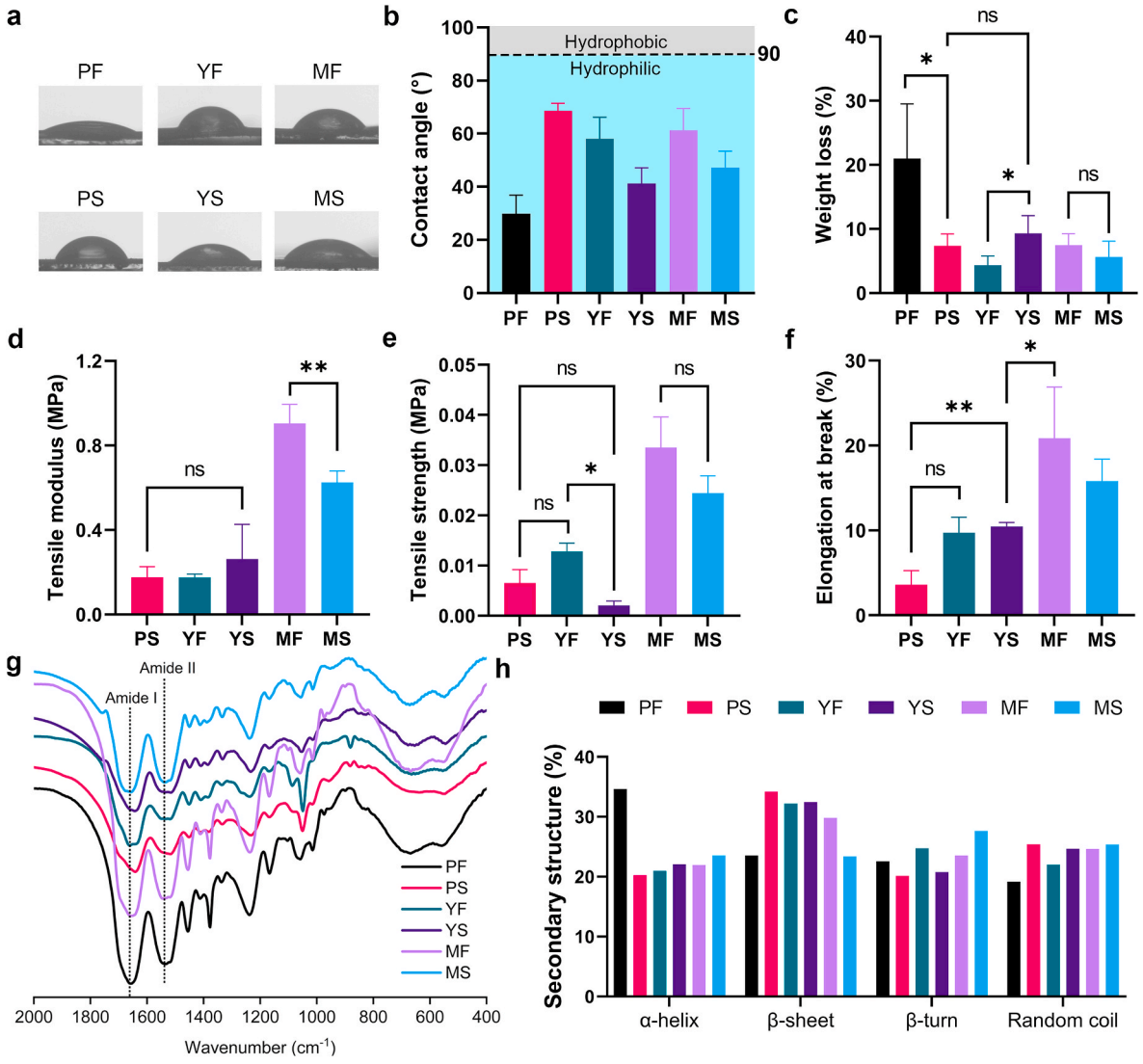

Fig. 2. Other physical properties of SF films remained similar following various treatments. (a,b) The contact angle of the SF films. (c) Weight loss of the SF films immersed in phosphate-buffered saline (PBS) for 24 h. (d–f) Mechanical properties of the SF films determined in wet conditions. (d) Tensile modulus, (e) Tensile strength, (f) Elongation at break. Data are expressed as mean ± SD (n = 5). (g) FTIR spectra of the SF films in a dry state. (h) The secondary structure percentage of the SF films calculated by deconvolution of the FTIR spectra. *$p < 0.05$, **$p < 0.01$, one-way ANOVA with Tukey post-hoc test. ns: not significant. PF: as cast fast drying film, PS: as cast slow drying film, YF: salting out-treated fast drying film, YS: salting out-treated slow drying film, MF: methanol-soaked fast drying film, MS: methanol-soaked slow drying film.

that these SF films can support cellular proliferation without inducing significant cytotoxicity. Next, the polarization state of RAW 264.7 cells grown on SF films was determined. iNOS and Arg1 were used as M1 and M2 macrophage markers, respectively. Typical M1-or M2-polarized macrophages can be induced by lipopolysaccharide (LPS) or IL4+IL13 treatment, respectively (Fig. 3a). Then, the expression levels of iNOS and Arg1 of RAW 264.7 cells on SF films were detected by western blot and immunofluorescence (Fig. 3b–f). Both results showed that the PS film induced the up-regulation of Arg1 while the YS film induced the up-regulation of iNOS. Similarly, the levels of CD80 and CD206, two cellular surface markers for M1 and M2 phenotype, were analyzed by flow cytometry (Fig. S5). Furthermore, pro-inflammatory (TNF-α, IL-6) and anti-inflammatory (IL-10, TGF-β) cytokines secreted by RAW 264.7 cells on SF films were quantified by ELISA (Fig. 3e–h). The level of TNF-α and IL-6 in YS-treated cells was 11.7-fold and 5.7-fold than the level in PS film-treated cells, respectively. In contrast, IL-10 and TGF-β levels were the highest in macrophages grown on the PS film. Meanwhile, the gene expression of these cytokines was also determined (Fig. S6). Together, the data indicates that the PS film with high roughness induced M2-like macrophages, whereas the YS film with low roughness induced M1-like macrophages.

To understand how the SF films induce differential macrophage polarization, the total mRNA expression of RAW 264.7 cells cultured on the SF films was analyzed by RNA sequencing. First, we compared sample differences by principal component analysis (PCA) (Fig. 4a). Following LPS or IL4+IL13 treatment, M1 and M2 macrophages shifted away from the TCP group in different indirections, respectively. It indicated that M1 and M2 macrophages have distinct transcriptomic profiles. Macrophages on SF films also displayed different profiles. Specifically, YS, YF, and MF film-cultured cells were clustering closely. PS and MS film-treated macrophages were shifting away from both M1 and M2. As shown in Fig. S7, the volcano plots showed 1168 up-regulated and 2247 down-regulated genes (TCP versus M1), 231 up-regulated and 260 down-regulated genes (TCP versus M2). Compared with TCP, the five SF films all induced a wide range of gene expression differences in macrophages. Since the PS film with high roughness polarized macrophages to M2-like and the YS film with low roughness polarized to M1-like, we chosen the two SF films for further

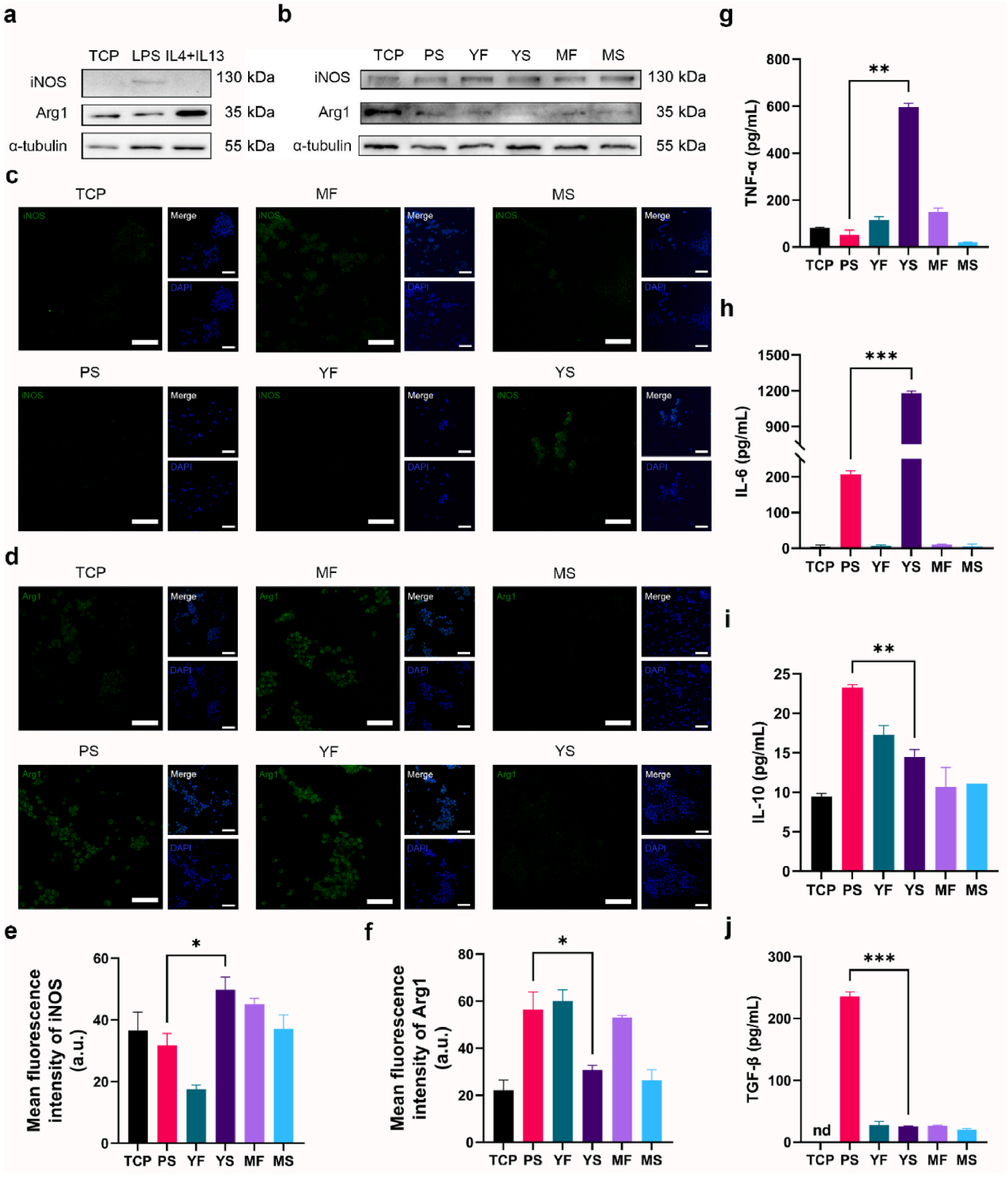

Fig. 3. Differential macrophage polarization modulated by different SF films. (a) Western blot images of iNOS and Arg1 expression of RAW 264.7 cells induced by lipopolysaccharide (LPS) and IL-4+IL-13 (20 ng/mL) for 24 h. (b) Western blot images of iNOS and Arg1 expression of RAW 264.7 cells on SF films for 24 h. (c,d) Immunofluorescent images of iNOS (c) and Arg1 (d) expression of RAW 264.7 cells on the SF films for 24 h. Scale bar, 50 μm. (e, f) Mean fluorescence intensity of iNOS (e) and Arg1 (f). (g–j) Cytokine levels secreted by RAW 264.7 cells induced by different SF films. (g) TNF-α, (h) IL-6, (i) IL-10, (j) TGF-β. Data are expressed as mean ± SD (n = 3). *$p < 0.05$, **$p < 0.01$, ***$p < 0.001$, two-tailed student's t-test. nd, not detected. PS: as cast slow drying film, YF: salting out-treated fast drying film, YS: salting out-treated slow drying film, MF: methanol-soaked fast drying film, MS: methanol-soaked slow drying film.

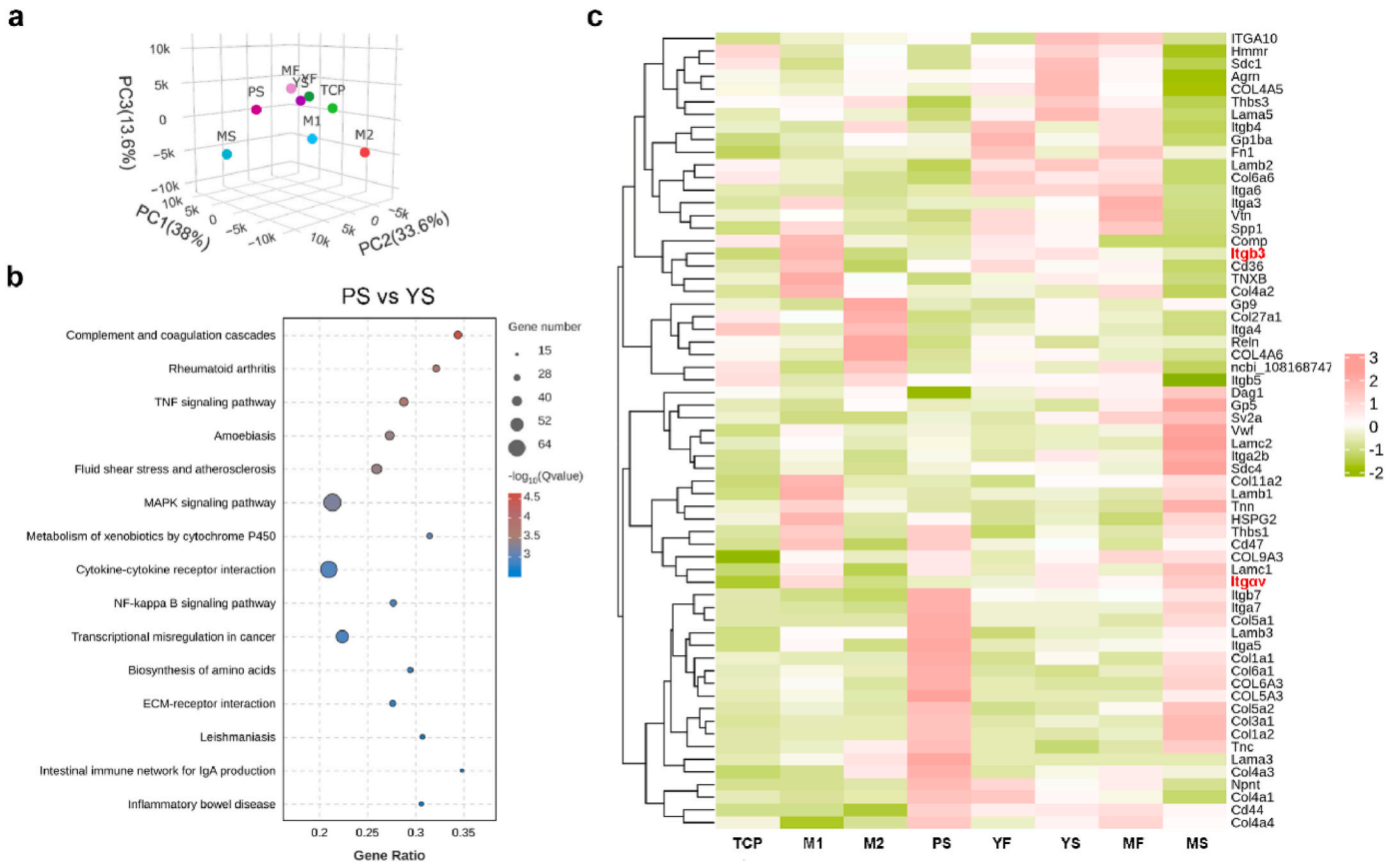

Fig. 4. Transcript sequence analysis of macrophage gene expression on the SF films. (a) Principal component analysis (PCA) of samples from macrophages with different treatments. (b) KEGG analysis of different signaling pathways between PS and YS films. (c) The heatmap of differential genes involved in ECM-receptor interactions. TCP: tissue culture plate. M1: LPS-treated RAW 264.7 cells. M2: IL4+IL13-treated RAW 264.7 cells. PS: as cast slow drying film, YF: salting out-treated fast drying film, YS: salting out-treated slow drying film, MF: methanol-soaked fast drying film, MS: methanol-soaked slow drying film.

transcriptome analysis. The Kyoto Encyclopedia of Genes and Genomes (KEGG) was performed to analyze the underlying signaling pathways. The top enriched up-KEGG pathways were shown in Fig. 4b. Compared with the PS film, the YS film-cultured macrophages displayed more inflammatory-related pathways. The data is in accordance with film-induced macrophage polarization. Given the differences in surface topology between PS and YS films, we analyzed the extracellular matrix (ECM)-cell interaction-related gene expressions. These differential gene expressions on ECM-receptor interaction were shown in the resulting heatmap (Fig. 4c). We noted that integrin αvβ3 was up-regulated in M1 macrophages and down-regulated in M2 macrophages. Meanwhile, the expression of *Itgav* and *Itgb3* was up-regulated in YS film-treated macrophages and down-regulated in PS film-treated macrophages. As integrin-based molecular complexes act as sensors to transmit extracellular environment signals, including physical and chemical properties of natural ECM or artificial substrates, to the intracellular modules, we focused on integrin receptors to investigate the mechanism of surface roughness on macrophage polarization.

2.3. Surface roughness increases plasma membrane curvature-mediated signaling to polarize macrophages

To confirm the expression difference in the protein level, αvβ3 expression in RAW 264.7 cells on PS and YS films was determined. The αv expression in YS film-treated macrophages was indeed higher than PS film-treated counterparts (Fig. 5a). Meanwhile, the cellular distribution of αv integrin by immunofluorescence confirmed these results (Fig. 5b and c). It suggested that the PS film with a rough surface can decrease the level of αv integrin, compared with the YS film of a relatively smooth surface. We then examined the protein expression of focal adhesion kinase (FAK) and nuclear factor-kappa B (NF-κB), two essential downstream signaling molecules, in macrophages on the PS and YS films. As shown in Fig. 5d–f, the expression level of phosphorylated-FAK in YS-treated cells was slightly higher than that in PS-treated cells ($p = 0.0583$). Meanwhile, phosphorylated–NF–κB in YS-treated cells also increased ($p < 0.05$). To explore the association between surface roughness and integrin αv expression, we hypothesized that surface roughness may manipulate integrin αv expression through plasma membrane curvature. To observe the macrophage-SF film interface, we employed a thin-section transmission electron microscope (TEM) to investigate the sections of PS/YS SF films and RAW 264.7 cells on these films. As shown in Fig. 5g, the PS film exhibited more curved surfaces than the YS film. When macrophages were cultured on the two films, cells could adhere to the films and adapt to the distinct surfaces (Fig. 5h). The curvature of the plasma membrane increased with the roughness of the SF films (Fig. 5i).

It is reported that the formation of positive membrane curvature of a cell can promote cellular endocytosis [36–38]. Therefore, we asked if increased membrane curvature in the PS film could lead to lysosomal degradation of integrin αv. By comparing TEM images of the cell-film interface, clear endocytic pits can be visualized in PS film-cultured macrophages instead of YS film-treated cells (Fig. S8). Also, the number and mass of lysosomes in macrophages cultured on the PS film were markedly higher than the YS film (Fig. S9), implying the improved degradation capability in macrophages on the PS film. Furthermore, we assessed the colocalization of integrin αv with the endolysosomal system. It is revealed by immunofluorescence that the green fluorescence signal of integrin αv overlapped with the red fluorescence signal of

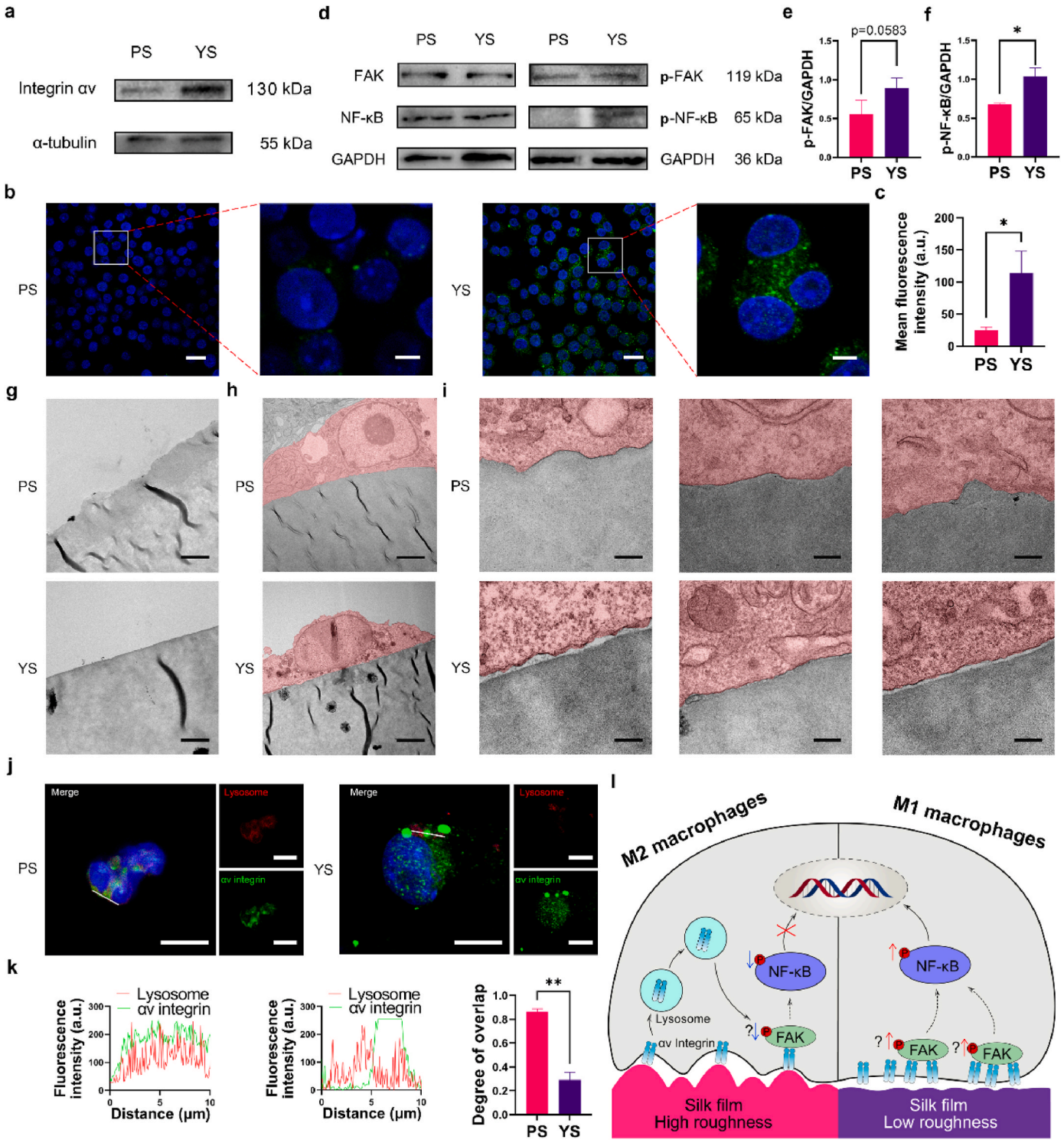

Fig. 5. Potential mechanism of surface roughness-induced macrophage polarization. (a) Western blot images of αv integrin expression in PS and YS film-treated RAW 264.7 cells for 24 h. (b) Immunofluorescent images of cellular distribution αv integrin in PS and YS film-treated RAW 264.7 cells. Scale bar in low magnification, 10 μm. Scale bar in high magnification, 5 μm. (c) Mean optical intensity of αv integrin from (b). (d) Western blot images of the expressions of FAK, phosphorylated-FAK, NF-κB, and phosphorylated–NF–κB in cells grown on PS and YS films. (e, f) Quantitative analysis of p-FAK and p–NF–κB in (d). (g) Thin-section transmission electron microscope (TEM) images of PS and YS films. Scale bar, 1 μm. (h,i) Thin-section TEM images of RAW 264.7 cell-PS/YS film interface. Cells were highlighted in red. Scale bar in (h), 5 μm. Scale bar in (i), 200 nm. (j,k) Co-localization of αv integrin and lysosomes in cells on PS and YS film-treated cells for 24 h. Scale bar, 10 μm. Lysosomes were stained by the lysotracker red dye. (l) Possible mechanism of the effect of surface roughness on macrophage polarization. Data are expressed as mean ± SD (n = 3). $*p < 0.05$, $**p < 0.01$, two-tailed student's t-test. PS: as cast slow drying film, YS: salting out-treated slow drying film.

lysosomes in PS film-treated macrophages (Fig. 5j and k). Taken together, the data suggests more integrin αv were trafficked into the endolysosomal system for degradation in PS film-cultured macrophages. Therefore, we revealed a preliminary mechanism for surface roughness-induced M2 macrophage polarization (Fig. 5l). On the rough PS film, macrophages deform the plasma membranes to adapt to the film surface. Thus, the membrane curvature elicits the endocytosis of integrin αv and subsequent lysosomal degradation. This upstream molecular event led to the inhibition of phosphorylation of NF-κB, which could be resulted from the down-regulation of p-FAK.

2.4. SF films with distinct surface roughness regulate the inflammatory response in vivo

To explore the in vivo macrophage polarization effect induced by surface roughness, the inflammatory response of the PS and YS films was investigated in a subcutaneous implantation mice model. We evaluated the skin tissues surrounding PS and YS films post-implantation for 3 days and 7 days. As revealed by hematoxylin-eosin (H&E) staining, a substance of inflammatory cells was distributed at the interface between tissue and YS film on day 3. In contrast, less infiltration of inflammatory cells can be observed with PS film-implanted tissue (Fig. 6a), as a significantly lower density of inflammatory cells was quantified in the PS group ($p < 0.05$) (Fig. 6b). Accompanied by inflammatory cellular infiltration, a dense fibrin layer deposited surrounded the YS film. However, the PS film induced less fibrin deposition (Fig. 6a), as shown by smaller fibrous capsule thickness and area ($p < 0.05$) (Fig. 6c and d). On day 7, the differences in the infiltration of inflammatory cells and fibrous capsule formation between the PS film and the YS film disappeared ($p > 0.05$) (Fig. 6e–g). Meanwhile, we characterized the distribution of F4/80+ macrophages infiltrated around the SF films (Fig. 6h and i), which was in agreement with the H&E analysis. Next, we evaluated the phenotype of macrophages infiltrated around the SF films by immunofluorescence staining. On day 3, Arg1+ macrophages infiltrated around the PS film. Instead, iNOS+ macrophages dominated around the YS film. On day 7, however, both Arg1+ and iNOS+ macrophages can be observed around the PS and YS films (Fig. 6j and k). These results indicated that the PS film with high roughness induced a weaker inflammatory response than the YS film with low roughness at the early stage of implantation.

3. Discussion

Over the last decade, a plethora of reports have demonstrated that the physical properties of a medical material have a huge influence on the polarization state of macrophages. Nevertheless, it is difficult to reach a consensus on the effect of a specific physical parameter on polarization direction. In this study, we employed several techniques to prepare and screen SF films with distinct surface roughness while keeping other physical properties invariable. To prepare water-insoluble SF films, slow-drying casting was employed to induce β-sheet structures in SF molecules. The resulting PS films exhibited marked surface nanostructures, which are similar to the structure of an SF film in a previous report [39]. Compared with traditional fast-drying casting, the slow-drying technique prolongs the water-SF molecule interaction, facilitating the transformation of water-soluble α-helix to insoluble β-sheets [40]. To some extent, this technique is like water vapor annealing, a typical post-treatment method to increase the water-insolubility of SF films [41]. Besides water annealing, exposure to organic solvents such as alcohols is another conventional way to construct water-stable SF films. Although the treatment of methanol markedly decreased the roughness of MF films, the mechanical properties of MF films also changed.

Salting out is often used to strengthen the mechanical properties of hydrogels [42,43]. We explored the possibility of salt soaking as a tool to tune the surface roughness of SF films. It turned out that this approach can modify the roughness of SF films in the nanoscale, despite no notable changes in mechanical properties. From soluble PF film to insoluble YF film, $(NH_4)_2SO_4$-induced conformational transition of SF molecules may play a dominant role in increasing the surface roughness of YF film. On the other hand, compared with the PS film, the YS film showed a declined surface roughness. As both NH_4^+ and SO_4^{2-} are strongly cosmotropic ions in the Hofmeister series, they can also actively interact with negatively-charged carboxyl and positively-charged amino groups in SF molecules. The interactions could be one of the possible reasons for declined roughness in YS films [44,45].

Besides surface roughness, surface properties of a biomaterial also cover surface charge, surface chirality, and so on [3]. As the chemical components of these SF films barely altered, the surface charge and chirality of the SF films by different treatments are expected to be stable.

We revealed that rough SF film PS can skew macrophages into M2-like phenotype while less rough SF film YS skews them in the opposite direction. This finding is in accordance with previous reports supporting that hydrophilic and rough surfaces promote anti-inflammatory differentiation of macrophages [8,10–15,24,25,46,47]. Given the important roles integrins play in sensing and transmitting outside signals, we screened integrin αvβ3 via transcriptome analysis as a target molecule to explore the mechanism of surface roughness on manipulation of macrophage polarization. The integrin αv expression in RAW 264.7 cells declined on the PS film while elevated on the YS film at both transcriptional and protein levels. Meanwhile, the downstream signaling molecules including p-FAK and p-NF-κB were activated with elevated αv expression in YS film-treated macrophages. The data can be supported by the fact that αvβ3-integrin signaling can active NF-κB-mediated inflammatory responses [48–51] and blocking αvβ3 can inhibit the phosphorylation of NF-κB [52,53]. Similarly, the inhibition of αvβ3-FAK-NF-κB signaling can be observed in M2-polarized macrophages cultured on modified titanium surfaces [23,54]. However, the expression of αvβ3 was up-regulated in M2-polarized macrophages induced by L-chiral nanoparticle-modified hydrogels [55]. This discrepancy implies that there may exist other signal molecules initiating macrophage polarization.

Currently, Wnt signaling [24,25] and autophagy pathway [11] have been proposed to explain the mechanism of increased surface roughness on M2-like macrophage polarization. However, the direct association between surface roughness and cellular signaling needs to be established. In the present study, we tried to connect material properties and signaling pathways from the perspective of membrane curvature. The membrane curvature is the spatial deformation or bending of plasma or organelle membranes, which plays a vital role in many cellular processes, including membrane trafficking, vesicle formation and fusion, and intracellular signaling [56,57]. When cells are cultured on substrates with nanostructures, the plasma membrane deforms and adheres to the substrates, generating a surface-induced membrane curvature at the cell-material interface [58]. In this study, the macrophages on SF films with different surface roughness showed divergent membrane curvatures. These observations are in good agreement with previous reports [36,37,59]. In addition, a highly positively-curved membrane of a living cell prefers endocytosis by recruiting endocytosis-related proteins [37,59,60]. Our data suggests the enhanced endocytosis of integrin αv in macrophages on the SF film with high roughness. Given autophagy is a lysosome-mediated degradative system [61] and the effect of autophagy on M2 polarization [62], we reason that curvature-mediated endocytosis and autophagy pathway may underlie the M2-polarized macrophages on rough SF films.

Despite the promising findings, this study has several limitations. First, due to the diversity of the Bin-Amphiphysin-Rvs (BAR) domain protein family which is responsible for sensing membrane curvatures, the effect of BAR domains on roughness-mediated endocytosis needs further evaluation. Secondly, as SF-based biomaterials are considered biodegradable, long-term implantation-induced in vivo biodegradation of the SF films will alter the surface roughness of these films. Thus, the

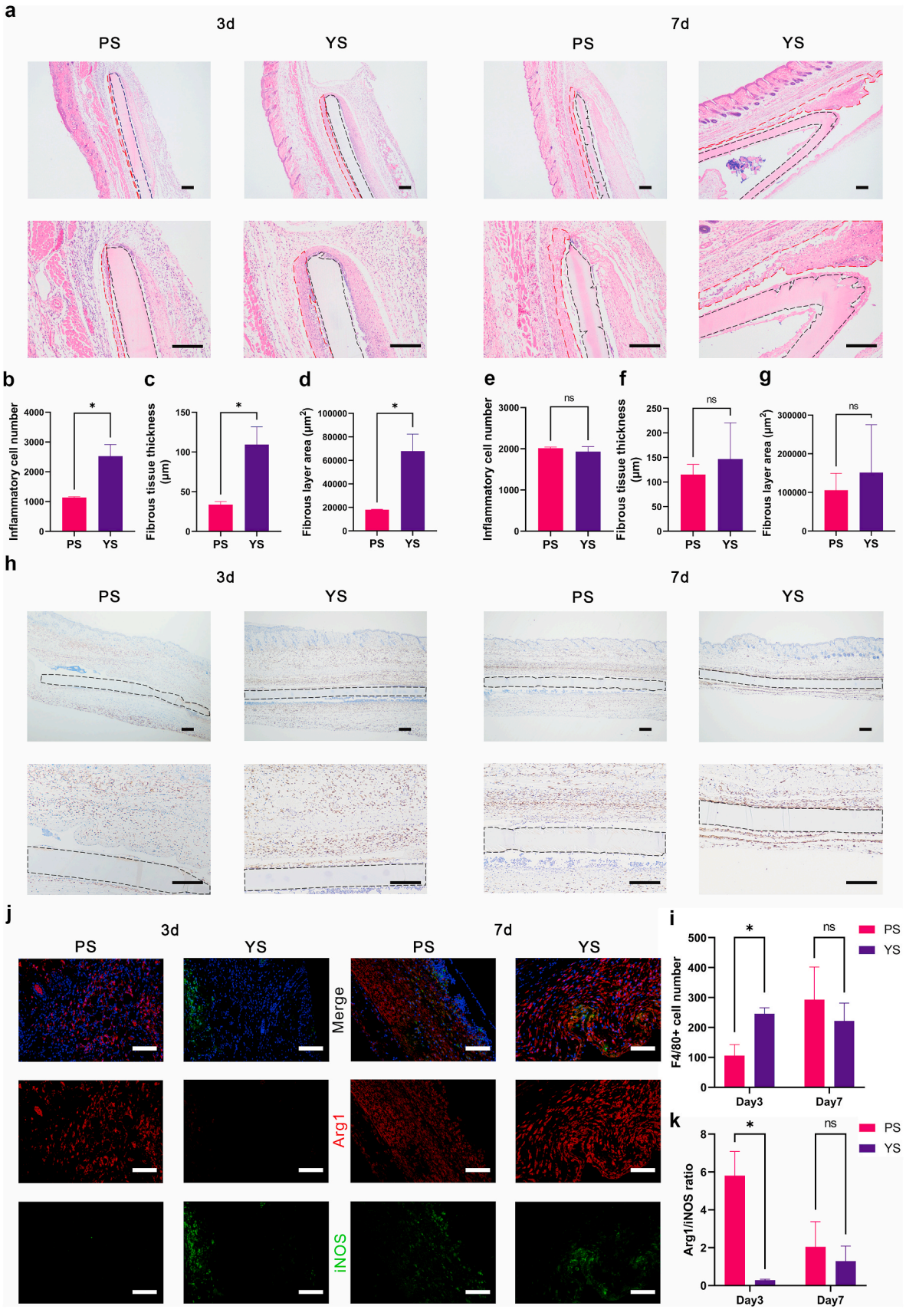

(caption on next page)

Fig. 6. Inflammatory response and macrophage distribution around SF films with distinct surface roughness in vivo. (a) Representative images of H&E staining of tissues surrounding PS and YS films after subcutaneously implanted in mice for 3 and 7 days. The black dotted lines and red dotted lines represent SF films and fibrous capsules, respectively. Scale bar, 200 μm. (b) Quantification of the infiltration of inflammatory cells with surface roughness on day 3 by H&E staining. (c, d) Quantification of the variation in fibrous capsule with surface roughness on day 3 by H&E staining. (e) Quantification of the infiltration of inflammatory cells with surface roughness on day 7 by H&E staining. (f, g) Quantification of the variation in fibrous capsule with surface roughness at day 7 by H&E staining. (h) Representative immunochemistry images by staining F4/80 positive macrophages on days 3 and 7. (i) Quantitative analysis of F4/80 positive macrophages on day 3 and 7. (j) Representative images of immunofluorescent staining of Arg1+ and iNOS+ macrophages on day 3 and 7. Scale bar, 200 μm. (k) Quantitative analysis of fluorescence intensity by immunofluorescent staining on day 3 and 7. Data are expressed as mean ± SD (n = 3). *$p < 0.05$, two-tailed student's t-test. ns, not significant.

dynamic topological changes of SF films induced by in vivo degradation should be investigated in the following study.

4. Conclusions

In conclusion, our work reveals the mechanism of surface roughness on macrophage polarization. We obtained SF films with tunable roughness and stable other physical parameters via slow-drying casting and salting out techniques. SF film with high roughness induced macrophages to differentiate to M2-like phenotype. In contrast, macrophages on less rough SF film acted in an M1-like phenotype. When implanted in mice, rough SF film effectively mitigates early inflammatory responses. Mechanically, the rough surface of SF film enabled a positively-curved membrane of macrophages, promoting the internalization and degradation of integrin αv and thus inhibiting the integrin–NF–κB signaling pathway. While SF film with low roughness activates the integrin–NF–κB signaling pathway. Our work facilitates a better understanding of the biomaterial-macrophage interface and SF films with tunable roughness can have a potential application in the regulation of inflammatory diseases.

5. Materials and methods

5.1. Chemicals

Silk cocoons of the silkworm Bombyx mori were given as gifts from Xinda Silk Co., Ltd (Guangdong, China). All chemicals and reagents were of analytical grade and used without further purification. Methanol was purchased from Sinopharm Chemical Reagents Co. Ltd., China. Ammonium sulfate ($(NH_4)_2SO_4$), Sodium carbonate (Na_2CO_3) and lithium bromide (LiBr) were purchased from Energy Chemical Co., Ltd. (Shanghai, China). Macrophage cell line RAW 264.7 was purchased from the National Collection of Authenticated Cell Cultures, China. Mouse fibroblast-like cells (L929) were kindly provided by the Institute of Applied Bioresource Research, Zhejiang University. IL4 and IL13 were purchased from PeproTech, Inc. Rabbit anti-iNOS antibody (#13120) and Alexa Fluor™ 488-conjugated goat anti-IgG secondary antibody (A11008) were purchased from Cell Signaling Technology. Inc. and Thermo Fisher Scientific, Inc., respectively. Lipopolysaccharide (LPS), rabbit anti-Arg1 antibody (AF1381), rabbit anti-Phospho–NF–κB p65 (Ser536) antibody (AN371), rabbit anti–NF–kB p65 antibody (AF1234), rabbit anti-Phospho-FAK (Tyr397) antibody (AF1960), rabbit anti-FAK antibody (AF1108), Lyso-Tacker red (C1046), and Actin-Tracker Green-488 (C2201S) were purchased from Beyotime Biotech. Inc. ELISA kits (TNF-α, IL-6, IL-10, TGF-β) were purchased from Elabscience, Inc. Integrin Alpha V Polyclonal antibody (27096-1-AP) was purchased from Proteintech Group, Inc. PE-conjugated anti-mouse CD206 (141705) and PE-conjugated anti-mouse CD80 (50-201-4699) antibodies were purchased from Biolegend, Inc, and Tonbo Biosciences, Inc, respectively.

5.2. Preparation and purification of SF aqueous solution

In brief, *B. mori* cocoons were boiled for 1 h in an aqueous solution of 0.02 M Na_2CO_3 and then rinsed thoroughly with pure water. After drying, the extracted silk fibroin was dissolved in 9.3 M LiBr solution at 60 °C for 4 h. This solution was dialyzed against deionized water using a dialysis cassette (MWCO 3500 Da) for 3 days to remove salts. The solution was optically clear after dialysis and was centrifuged to remove the small amounts of silk aggregates. The final concentration of the SF aqueous solution was 8 % (w/v), which was determined by weighing the residual solid from a known volume of solution after drying at 60 °C.

5.3. Preparation of SF films

The resulting SF solutions were cast onto Petri dishes to obtain SF films by drying them at room temperature in a fume hood. Fast-dried films (PF) and slowly-dried SF films (PS) were obtained by modulating the airflow speed in the fume hood. Then, these SF films were exposed to $(NH_4)_2SO_4$ (2 M) aqueous solution or 80 % (w/v) methanol for 48 h or 24 h, respectively. The resulting films, including fast-dried films treated with $(NH_4)_2SO_4$ (YF), fast-dried films treated with methanol (MF), slowly-dried films treated with $(NH_4)_2SO_4$ (YS), and slowly-dried films treated with methanol (MS), were washed and dried for use.

Spectrophotometry was employed to detect the possible $(NH_4)_2SO_4$ and methanol residues. $(NH_4)_2SO_4$ was determined by barium chromate spectrophotometry [63]. A standard curve has been obtained as $y = 0.0001x+0.0686$ ($R^2 = 0.9125$), where y is the OD value at 420 nm and x is the concentration of ammonium sulfate (x = 0–264 μg/mL). The concentration of $(NH_4)_2SO_4$ in the leaching solution was calculated to be 4.8 ± 0.56 μg/mL. Treatment of $(NH_4)_2SO_4$ at 50 μg/mL does not induce iNOS expression in RAW264.7 cells (data not shown). Methanol was detected by the chromotropic acid method [64]. A standard curve has been obtained as $y = 0.0007x+0.0972$ ($R^2 = 0.9294$), in which y is OD value at 570 nm and x is the concentration of methanol (x = 0–600 ng/mL). No methanol can be detected.

5.4. Characterization of SF films

Surface morphology. The surface morphology of SF films was observed by scanning electron microscopy (SEM) (Zeiss, Germany) and atomic force microscopy (AFM) (Dimension Icon, Bruker, US). Solubility test. SF films were cut into squares (10 × 10 mm). The samples were weighed (W1) and immersed in PBS for incubation at 37 °C for 24 h. Then, the samples were harvested and transferred to an oven before weighing the dried films (W2). The leaching loss percentage was calculated according to Eq. (1).

$$w = W2/W1 \times 100\% \quad (1)$$

Water contact angle measurement. The hydrophobic or hydrophilic characteristics of different SF films were determined by an automatic contact angle meter (Dataphysics, OCA20, Germany). Photographs were taken after the droplet had settled on the surface (time >15 s) for further analysis. Mechanical test. The tensile properties of different SF films were measured on a universal testing machine (UTM4204, Suns, China) at 25 °C and a relative humidity of 60 %. The SF films were cut into 30 × 10 mm strips and soaked in PBS before testing. The strain rate was set at 5 mm/min. The stress-strain curves for the samples were obtained from the recorded load-deformation curves. The Young's modulus, ultimate tensile strength and strain to failure were the average of 5 measurements. Fourier Transform Infrared Spectroscopy (FTIR). FTIR spectra of the SF films were obtained with an FTIR spectrometer (VERTEX 70, Bruker, US) in the range 4000-400 cm^{-1}. Before the measurement, KBr

pellets were prepared by mixing SF films and KBr in the mass ratio of 1:100 (w/w).

5.5. Cell culture

RAW 264.7 and mouse fibroblast-like cells (L929) cells were cultured in high glucose DMEM supplemented with 10 % FBS and 1 % penicillin/streptomycin at 37 °C in the presence of 5 % CO_2.

5.6. Cell counting kit-8 (CCK8) assay

Cell proliferation on the SF films was detected by CCK8 assay. SF films were cut into circular pieces with diameters of 6.4 mm, which were then soaked in PBS for UV irradiation. SF films were placed genteelly in the 96-well plate, with the front side of the films upward. Cell suspensions of RAW 264.7 and L929 (5×10^3/well) were seeded onto the SF films and incubated for 24 h. Then, cell proliferation was evaluated according to the manufacturer's protocol.

5.7. Western blot

SF films were cut into circular pieces with diameters of 35 mm, and soaked in PBS for UV irradiation before transferring to a 6-well plate. RAW 264.7 cells were seeded in the SF film-coated plate and incubated for 24 h. Tissue culture plate (TCP), LPS (500 ng/mL), and IL4+IL13 (20 ng/mL) without film coating were used as controls. Then, cells were harvested from the SF films for western blotting. Total protein from the cells was extracted and the content was measured by a BCA protein assay kit. The proteins were separated on an SDS-PAGE gel, transferred to a poly (vinylidene difluoride) (PVDF) membrane, and incubated with primary antibodies against iNOS, Arg1, α-tubulin at 4 °C overnight. Then, the PVDF membrane was incubated with a secondary antibody and visualized with an electrochemiluminescence detection reagent.

5.8. Immunofluorescence assay and flow cytometry

To visualize the expression of polarization markers of RAW 264.7 cells, the cells grown on different SF films (10 × 10 mm) were fixed in 4 % paraformaldehyde for 10 min, permeabilized with 0.1 % Triton X-100 for 5 min and blocked with 1 % BSA for 30 min. Following washing with PBS, the cells on SF films were incubated overnight at 4 °C with the primary antibody against iNOS, Arg1, integrin αv. Then, the cells were incubated with Alexa Fluor™ 488-conjugated secondary antibody at room temperature and stained with Hoechst 33342. The SF films were placed on the slides and sealed with 60 % glycerin before imaging by CLSM. To label lysosomes, cells were incubated first with Lyso-Tracker Red at 37 °C for 30 min before fixation. For flow cytometry, RAW 264.7 cells were grown on SF films with a density of 2×10^5/well. Following 24 h, cells on SF films were harvested and incubated with PE-CD80 or PE-CD206 at 4 °C for 15 min. Then, the cells were washed and analyzed by flow cytometry.

5.9. Enzyme-linked immunosorbent assay (ELISA) and RT-qPCR

SF films were cut into circular pieces with diameters of 35 mm, and soaked in PBS for UV irradiation before transferring to a 6-well plate. SF films were incubated with fresh DMEM at 37 °C overnight followed by RAW 264.7 cell seeding. Then, RAW 264.7 cells were incubated on the SF films for 24 h before harvesting the supernatant. The supernatant was used for cytokine measurement (TNF-α, IL-6, IL-10, and TGF-β), according to the manufacturer's protocols (Elabscience, China). To determine the gene expression of these cytokines, real-time quantitative polymerase chain reaction (RT-qPCR) was performed. The total RNA was extracted from SF film-treated RAW 264.7 cells. Reverse transcription was performed from the total RNA using PrimeScript™ RT Master Mix (RR047A). The primers used in this section are listed in Table S1.

5.10. RNA sequencing

The total RNA samples from RAW 264.7 cells were extracted from cells cultured on SF films. RNA sequencing was performed by Gene Denovo Biotechnology Co., Ltd (Guangzhou, China). All data analysis was performed by Omicsmart Cloud Platform (www.omicsmart.com). The screening threshold for the differentially expressed genes (DEGs) was set to absolute fold change >2, Q value < 0.05, and false discovery rate (FDR) below 0.1. The differentially expressed genes were mapped to Gene Ontology (GO) terms in the Gene Ontology database and subjected to pathway enrichment analysis.

5.11. Transmission electron microscope (TEM) for the interface of SF films and cells

RAW 264.7 cells cultured on the SF films were prepared for thin-section TEM by fixing in 2.5 % glutaraldehyde in PBS (pH 7.4), rinsing four times in PBS, and staining in 1 % osmium tetroxide in PBS and 1 % uranyl acetate in double distilled water overnight. Then the samples were rinsed four times in double distilled water. Cells were dehydrated in 30, 50, 70, 85, 95, and 100 % ice-cold ethanol and infiltrated in Spurr resin. The resin was polymerized in a 70 °C oven for 24 h, and 70 nm sections were cut with an ultramicrotome (UC7, Leica). The specimen sections were poststained with 2 % uranyl acetate and alkaline lead citrate and imaged in TEM of Model Talos L120C (Thermo Fisher Scientific).

5.12. In vivo subcutaneous implantation

C57BL/6 female mice aged 8 weeks were obtained from Bestest Biotechnology Co., Ltd (Zhuhai, China). All the procedures of the experiments were approved by South China Agricultural University and conducted regarding the guidelines of laboratory animal care and use (Application number: 2023B154). Three replicates for each type of SF film were implanted into mice. Before surgery, anesthesia was induced. The dorsal surface of each mouse was shaved, sterilized with betadine solution, and washed with sterile PBS. About a 10 mm incision was made in the skin to form subcutaneous pockets. Before implantation, SF films with a diameter of 6.5 mm were sterilized with 75 % ethanol. Then, the films were inserted into the incisions. After implantation, the incisions were closed with wound clips. Mice were monitored until recovery from anesthesia and housed for 3 and 7 days.

5.13. Histological analysis, macrophage immunochemistry and immunofluorescence

After each time point, mice were sacrificed and the SF film samples together with the surrounding tissue were excised and collected. The samples were fixed in 4 % paraformaldehyde overnight and embedded in paraffin wax. Sections of each sample at 3–5 μm thickness were cut and mounted onto slides. The sections were stained with hematoxylin and eosin (H&E) to evaluate the fibrotic capsule and inflammatory cell infiltration around SF films. The macrophage infiltration at the implant surface was detected via immunochemistry staining of macrophage marker F4/80. The macrophage phenotype was detected by immunofluorescence staining. M1 and M2 macrophages were marked by iNOS and Arg1. H&E images and immunochemistry images were obtained by light microscopy, while immunofluorescence images were obtained by fluorescence microscopy. Image J software was utilized for quantification analysis.

5.14. Statistical analysis

Data were reported as mean ± standard deviation (SD). All statistical

comparisons and nonlinear regressions were performed in Prism 8.3 (GraphPad Software, Inc.). One-way analysis of variance (ANOVA) or student's t-test was used to compare data from more than two groups. p-value <0.05 was considered to be statistically significant.

CRediT authorship contribution statement

Doudou Hu: Writing – review & editing, Writing – original draft, Methodology, Formal analysis, Conceptualization. **Tiandong Li:** Visualization, Validation, Investigation, Formal analysis. **Haixu Bian:** Formal analysis. **Haiyu Liu:** Investigation. **Pengwei Wang:** Investigation. **Yeyuan Wang:** Resources. **Jingchen Sun:** Writing – review & editing, Supervision.

Declaration of competing interest

The authors declare that they have no known competing financial interests or personal relationships that could have appeared to influence the work reported in this paper.

Data availability

Data will be made available on request.

Acknowledgments

We thank Chuanhe Liu at South China Agricultural University for the help on sample preparation for thin-section TEM. This work was supported by the Guangdong Basic and Applied Basic Research Foundation (2022A1515110329).

Appendix A. Supplementary data

Supplementary data to this article can be found online at https://doi.org/10.1016/j.mtbio.2024.101193.

References

[1] A. Wynn Thomas, M. Vannella Kevin, Macrophages in tissue repair, regeneration, and fibrosis, Immunity 44 (2016) 450–462.
[2] Peter J. Murray, Macrophage polarization, Annu. Rev. Physiol. 79 (2017) 541–566.
[3] Li Jinhua, Xinquan Jiang, Li Hongjun, Gelinsky Michael, Zhen Gu, Tailoring materials for modulation of macrophage fate, Adv. Mater. 33 (2021) 2004172.
[4] O. Abaricia Jefferson, Farzad Negin, J. Heath Tyler, Jamelle Simmons, Morandini Lais, Olivares-Navarrete Rene, Control of innate immune response by biomaterial surface topography, energy, and stiffness, Acta Biomater. 133 (2021) 58–73.
[5] Sayan Deb Dutta, Ganguly Keya, Tejal V. Patil, Randhawa Aayushi, Lim Ki-Taek, Unraveling the potential of 3D bioprinted immunomodulatory materials for regulating macrophage polarization: state-of-the-art in bone and associated tissue regeneration, Bioact. Mater. 28 (2023) 284–310.
[6] Ben Zhang, Yingchao Su, Juncen Zhou, Zheng Yufeng, Donghui Zhu, Toward a better regeneration through implant-mediated immunomodulation: harnessing the immune responses, Adv. Sci. 8 (2021) 2100446.
[7] Katrin A. Barth, Waterfield J. Douglas, Donald M. Brunette, The effect of surface roughness on RAW 264.7 macrophage phenotype, J. Biomed. Mater. Res. 101 (2013) 2679–2688.
[8] M. Hotchkiss Kelly, M. Clark Nicholas, Olivares-Navarrete Rene, Macrophage response to hydrophilic biomaterials regulates MSC recruitment and T-helper cell populations, Biomaterials 182 (2018) 202–215.
[9] Shayan Mahdis, Padmanabhan Jagannath, Aaron H. Morris, Bettina Cheung, Ryan Smith, Schroers Jan, R. Kyriakides Themis, Nanopatterned bulk metallic glass-based biomaterials modulate macrophage polarization, Acta Biomater. 75 (2018) 427–438.
[10] He Ye, Xu Kun, Li Ke, Yuan Zhang, Ding Yao, Maowen Chen, Chuanchuan Lin, Tao Bailong, Li Xuemin, Guanjun Zhang, Improved osteointegration by SEW2871-encapsulated multilayers on micro-structured titanium via macrophages recruitment and immunomodulation, Appl. Mater. Today 20 (2020) 100673.
[11] Jing Luo, Yide He, Fanhui Meng, Ning Yan, Yumei Zhang, Wen Song, The role of autophagy in M2 polarization of macrophages induced by micro/nano topography, Int. J. Nanomed. (2020) 7763–7774.
[12] Sanghun Lee, Junggeon Park, Semin Kim, Jehyung Ok, Yoo Jung Il, Kim Yong Sook, Youngkeun Ahn, Kim Tae-il, Ko Heung Cho, Lee Jae Young, High-performance implantable bioelectrodes with immunocompatible topography for modulation of macrophage responses, ACS Nano 16 (2022) 7471–7485.
[13] Jiaqi Shao, Luxi Weng, Li Juan, Huiping Lin, Huiming Wang, Jun Lin, Regulation of macrophage polarization by mineralized collagen coating to accelerate the osteogenic differentiation of mesenchymal stem cells, ACS Biomater. Sci. Eng. 8 (2022) 610–619.
[14] Menglu Wang, Fuying Chen, Yitao Tang, Wang Jing, Xuening Chen, Li Xiangfeng, Zhang Xingdong, Regulation of macrophage polarization and functional status by modulating hydroxyapatite ceramic micro/nano-topography, Mater. Des. 213 (2022) 110302.
[15] M. Hotchkiss Kelly, B. Reddy Gireesh, L. Hyzy Sharon, Zvi Schwartz, D. Boyan Barbara, Olivares-Navarrete Rene, Titanium surface characteristics, including topography and wettability, alter macrophage activation, Acta Biomater. 31 (2016) 425–434.
[16] Ma Qian-Li, Zhao Ling-Zhou, Liu Rong-Rong, Jin Bo-Quan, Song Wen, Wang Ying, Zhang Yu-Si, Chen Li-Hua, Zhang Yu-Mei, Improved implant osseointegration of a nanostructured titanium surface via mediation of macrophage polarization, Biomaterials 35 (2014) 9853–9867.
[17] Li Xuezhong, Huang Qianli, Elkhooly Tarek A, Liu Yong, Wu Hong, Feng Qingling, Ling Liu, Yu Fang, Weihong Zhu, Hu Tianrui, Effects of titanium surface roughness on the mediation of osteogenesis via modulating the immune response of macrophages, Biomed. Mater. 13 (2018) 045013.
[18] Li Jun, Zhang Yu-Jue, Lv Zhao-Yong, Kun Liu, Meng Chun-Xiu, Bo Zou, Li Ke-Yi, Liu Feng-Zhen, Zhang Bin, The observed difference of macrophage phenotype on different surface roughness of mineralized collagen, Regenerative Biomaterials 7 (2020) 203–211.
[19] Jinjin Wang, Meng Fanhui, Song Wen, Jingyi Jin, Ma Qianli, Fei Dongdong, Fang Liang, Lihua Chen, Wang Qintao, Zhang Yumei, Nanostructured titanium regulates osseointegration via influencing macrophage polarization in the osteogenic environment, Int. J. Nanomed. (2018) 4029–4043.
[20] Segan Sören, Jakobi Meike, Khokhani Paree, Klimosch Sascha, Billing Florian, Schneider Markus, Martin Dagmar, Metzger Ute, Biesemeier Antje, Xiong Xin, Systematic investigation of polyurethane biomaterial surface roughness on human immune responses in vitro, BioMed Res. Int. 2020 (2020).
[21] Li Linhao, Yuna Qian, Chao Jiang, Yonggang Lv, Wanqian Liu, Li Zhong, Kaiyong Cai, Li Song, Li Yang, The use of hyaluronan to regulate protein adsorption and cell infiltration in nanofibrous scaffolds, Biomaterials 33 (2012) 3428–3445.
[22] Nianji Yang, Matthew J. Moore, L. Michael Praveesuda, Miguel Santos, Yuen Ting Lam, Shisan Bao, Martin KC. Ng, Rnjak-Kovacina Jelena, Richard P. Tan, Steven G. Wise, Silk fibroin scaffold architecture regulates inflammatory responses and engraftment of bone marrow-mononuclear cells, Adv. Healthcare Mater. 10 (2021) 2100615.
[23] Lan Chen, Donghui Wang, Peng Feng, Jiajun Qiu, Liping Ouyang, Yuqin Qiao, Liu Xuanyong, Nanostructural surfaces with different elastic moduli regulate the immune response by stretching macrophages, Nano Lett. 19 (2019) 3480–3489.
[24] O. Abaricia Jefferson, H. Shah Arth, Chaubal Manotri, M. Hotchkiss Kelly, Olivares-Navarrete Rene, Wnt signaling modulates macrophage polarization and is regulated by biomaterial surface properties, Biomaterials 243 (2020) 119920.
[25] Avery Derek, Morandini Lais, Sheakley Luke S, H. Shah Arth, Bui Loc, O. Abaricia Jefferson, Olivares-Navarrete Rene, Canonical Wnt signaling enhances pro-inflammatory response to titanium by macrophages, Biomaterials 289 (2022) 121797.
[26] Hang Ruiyue, Zhao Yuyu, Zhang Yi, Runhua Yao, Yao Xiaohong, Yonghua Sun, Huang Di, Hang Ruiqiang, The role of nanopores constructed on the micropitted titanium surface in the immune responses of macrophages and the potential mechanisms, J. Mater. Chem. B 10 (2022) 7732–7743.
[27] Yide He, Luo Jing, Yinlong Zhang, Li Zhe, Fanghao Chen, Song Wen, Zhang Yumei, The unique regulation of implant surface nanostructure on macrophages M1 polarization, Mater. Sci. Eng. C 106 (2020) 110221.
[28] Jiamei Zhang, Lingshuang Wang, Xu Cheng, Yingui Cao, Shengsheng Liu, Rui L. Reis, Subhas C. Kundu, Xiao Yang, Bo Xiao, Lian Duan, Transparent silk fibroin film-facilitated infected-wound healing through antibacterial, improved fibroblast adhesion and immune modulation, J. Mater. Chem. B 12 (2024) 475–488.
[29] Yuping Chen, Hesong Wu, Tao Yang, Guanshan Zhou, Yuyin Chen, Jie Wang, Chuanbin Mao, Mingying Yang, Biomimetic nucleation of metal–organic frameworks on silk fibroin nanoparticles for designing core–shell-structured pH-responsive anticancer drug carriers, ACS Appl. Mater. Interfaces 13 (2021) 47371–47381.
[30] Santin Matteo, Motta Antonella, Freddi Giuliano, Cannas Mario, In vitro evaluation of the inflammatory potential of the silk fibroin, J. Biomed. Mater. Res. 46 (1999) 382–389.
[31] Meinel Lorenz, Hofmann Sandra, Karageorgiou Vassilis, Kirker-Head Carl, McCool John, Gronowicz Gloria, Zichner Ludwig, Langer Robert, Vunjak-Novakovic Gordana, David L. Kaplan, The inflammatory responses to silk films in vitro and in vivo, Biomaterials 26 (2005) 147–155.
[32] Yanan Zhang, Sheng Renwang, Jialin Chen, Hongmei Wang, Yue Zhu, Zhicheng Cao, Zhao Xinyi, Zhimei Wang, Chuanquan Liu, Zhixuan Chen, Silk fibroin and sericin differentially potentiate the paracrine and regenerative functions of stem cells through multiomics analysis, Adv. Mater. 35 (2023) 2210517.
[33] Roy Subhadeep, Sharma Aarushi, Ghosh Sourabh, Macrophage polarization profiling on native and regenerated silk biomaterials, ACS Biomater. Sci. Eng. 8 (2022) 659–671.
[34] Sapudom Jiranuwat, Kongsema Mesayamas, Methachittipan Apipon, Damrongsakkul Siriporn, Kanokpanont Sorada, C.M. Teo Jeremy, Khongkow Mattaka, Tonsomboon Khaow, Thongnuek Peerapat, Degradation

products of crosslinked silk fibroin scaffolds modulate the immune response but not cell toxicity, J. Mater. Chem. B 11 (2023) 3607–3616.
[35] Ziyang Sun, Ruochuan Huang, Hao Lyu, Yu Xin, Wenzhao Wang, Li Jinghang, Xingyu Lu, Chengchen Guo, Silk acid as an implantable biomaterial for tissue regeneration, Adv. Healthcare Mater. 12 (2023) 2301439.
[36] Gopal Sahana, Chiappini Ciro, Penders Jelle, Leonardo Vincent, Seong Hyejeong, Rothery Stephen, Korchev Yuri, Shevchuk Andrew, M. Stevens Molly, Porous silicon nanoneedles modulate endocytosis to deliver biological payloads, Adv. Mater. 31 (2019) 1806788.
[37] C. Cail Robert, R. Shirazinejad Cyna, David G. Drubin, Induced nanoscale membrane curvature bypasses the essential endocytic function of clathrin, J. Cell Biol. 221 (2022) e202109013.
[38] Zhao Wenting, Hanson Lindsey, Lou Hsin-Ya, Akamatsu Matthew, D. Chowdary Praveen, Santoro Francesca, Marks Jessica R, Grassart Alexandre, David G. Drubin, Cui Yi, Nanoscale manipulation of membrane curvature for probing endocytosis in live cells, Nat. Nanotechnol. 12 (2017) 750–756.
[39] Qiang Lu, Hu Xiao, Xiaoqin Wang, Jonathan A. Kluge, Shenzhou Lu, Cebe Peggy, David L. Kaplan, Water-insoluble silk films with silk I structure, Acta Biomater. 6 (2010) 1380–1387.
[40] Stengel Dillan, Addison J. Bennett, Onofrei David, Huynh Nha Uyen, Youssef George, Gregory P. Holland, Hydration-induced β-sheet crosslinking of α-helical-rich spider prey-wrapping silk, Adv. Funct. Mater. 31 (2021) 2007161.
[41] Hu Xiao, Shmelev Karen, Sun Lin, Gil Eun-Seok, Park Sang-Hyug, Cebe Peggy, David L. Kaplan, Regulation of silk material structure by temperature-controlled water vapor annealing, Biomacromolecules 12 (2011) 1686–1696.
[42] Hua Mutian, Shuwang Wu, Ma Yanfei, Zhao Yusen, Zilin Chen, Frenkel Imri, Strzalka Joseph, Hua Zhou, Xinyuan Zhu, He Ximin, Strong tough hydrogels via the synergy of freeze-casting and salting out, Nature 590 (2021) 594–599.
[43] Shuwang Wu, Mutian Hua, Alsaid Yousif, Yingjie Du, Yanfei Ma, Zhao Yusen, Lo Chiao-Yueh, Canran Wang, Wu Dong, Bowen Yao, Poly (vinyl alcohol) hydrogels with broad-range tunable mechanical properties via the Hofmeister effect, Adv. Mater. 33 (2021) 2007829.
[44] Klacić Tin, Bohinc Klemen, Kovacević Davor, Suppressing the hofmeister anion effect by thermal annealing of thin-film multilayers made of weak polyelectrolytes, Macromolecules 55 (2022) 9571–9582.
[45] Andreeva Tonya, Danailova Avgustina, Terziyska Penka, Krumova Shashka, Taneva Stefka, Krastev Rumen, Hofmeister anions effect on the thickness and morphology of polyelectrolyte multilayers for biofunctionalization of cardiovascular stents, Bulg. Chem. Commun. 48 (2016) 23–28.
[46] Zetao Chen, Bachhuka Akash, Shengwei Han, Wei Fei, Lu Shifeier, Visalakshan Rahul Madathiparambil, Vasilev Krasimir, Xiao Yin, Tuning chemistry and topography of nanoengineered surfaces to manipulate immune response for bone regeneration applications, ACS Nano 11 (2017) 4494–4506.
[47] Yide He, Li Zhe, Ding Xin, Xu Boya, Wang Jinjin, Li Yi, Fanghao Chen, Meng Fanhui, Song Wen, Yumei Zhang, Nanoporous titanium implant surface promotes osteogenesis by suppressing osteoclastogenesis via integrin β1/FAKpY397/MAPK pathway, Bioact. Mater. 8 (2022) 109–123.
[48] Gianni Tatiana, Leoni Valerio, Chesnokova Liudmila S, M. Hutt-Fletcher Lindsey, Campadelli-Fiume Gabriella, αvβ3-integrin is a major sensor and activator of innate immunity to herpes simplex virus-1, Proc. Natl. Acad. Sci. USA 109 (2012) 19792–19797.
[49] Jie Chen, Green Jonette, Jr Arif Yurdagul, Albert Patrick, Marshall C. McInnis, A Wayne Orr, αvβ3 integrins mediate flow-induced NF-κB Activation, proinflammatory gene expression, and early atherogenic inflammation, Am. J. Pathol. 185 (2015) 2575–2589.
[50] Wang Qian, Onuma Kazuhiro, Changhao Liu, Heidi Wong, Michelle S. Bloom, Eileen E. Elliott, Richard RL. Cao, Nick Hu, Lingampalli Nithya, Sharpe Orr, Dysregulated integrin αVβ3 and CD47 signaling promotes joint inflammation, cartilage breakdown, and progression of osteoarthritis, JCI Insight 4 (2019).
[51] S. Antonov Alexander, N. Antonova Galina, David H. Munn, Mivechi Nahid, Lucas Rudolf, D. Catravas John, D. Verin Alexander, αVβ3 integrin regulates macrophage inflammatory responses via PI3 kinase/Akt-dependent NF-κB activation, J. Cell. Physiol. 226 (2011) 469–476.
[52] H. Zhang, K. Zhang, Q.S. Zhang, L. Wang, Y.H. Gao, G.Y. Xu, D. Long, H. Wang, Y. Hu, A peptidic network antibody inhibits both angiogenesis and inflammatory response, J. Contr. Release 362 (2023) 715–725.
[53] Zhixia Chen, Xibing Ding, Shuqing Jin, Pitt Bruce, Liming Zhang, Billiar Timothy, Li Quan, WISP1-αvβ3 integrin signaling positively regulates TLR-triggered inflammation response in sepsis induced lung injury, Sci. Rep. 6 (2016) 28841.
[54] Xiaobin Guo, Jiaxiang Bai, Ge Gaoran, Zhidong Wang, Qing Wang, Kai Zheng, Tao Huaqiang, Lirong Zhang, Hongbo Zhang, Dongqing Wang, Bioinspired peptide adhesion on Ti implants alleviates wear particle-induced inflammation and improves interfacial osteogenesis, J. Colloid Interface Sci. 605 (2022) 410–424.
[55] Yide He, Xige Zhang, Meng Fanhui, Wang Jinjin, Li Yi, Zhang Yan, Song Wen, Li Tianjie, Zhang Yumei, Biomimetic chiral nanotopography for manipulating immunological response, Adv. Funct. Mater. (2023) 2313157.
[56] T. McMahon Harvey, L. Gallop Jennifer, Membrane curvature and mechanisms of dynamic cell membrane remodelling, Nature 438 (2005) 590–596.
[57] K. Jarsch Iris, Daste Frederic, L. Gallop Jennifer, Membrane curvature in cell biology: An integration of molecular mechanisms, J. Cell Biol. 214 (2016) 375–387.
[58] Lou Hsin-Ya, Zhao Wenting, Yongpeng Zeng, Bianxiao Cui, The role of membrane curvature in nanoscale topography-induced intracellular signaling, Accounts Chem. Res. 51 (2018) 1046–1053.
[59] Galic Milos, Jeong Sangmoo, Tsai Feng-Chiao, Joubert Lydia-Marie, Yi I. Wu, M. Hahn Klaus, Cui Yi, Tobias Meyer, External push and internal pull forces recruit curvature-sensing N-BAR domain proteins to the plasma membrane, Nat. Cell Biol. 14 (2012) 874–881.
[60] F. Zeno Wade, B. Hochfelder Jacob, S. Thatte Ajay, Liping Wang, K. Gadok Avinash, C. Hayden Carl, M. Lafer Eileen, C. Stachowiak Jeanne, Clathrin senses membrane curvature, Biophys. J. 120 (2021) 818–828.
[61] B. Birgisdottir Åsa, Johansen Terje, Autophagy and endocytosis–interconnections and interdependencies, J. Cell Sci. 133 (2020) jcs228114.
[62] K. Liu, E.P. Zhao, G. Ilyas, G. Lalazar, Y. Lin, M. Haseeb, K.E. Tanaka, M.J. Czaja, Impaired macrophage autophagy increases the immune response in obese mice by promoting proinflammatory macrophage polarization, Autophagy 11 (2015) 271–284.
[63] S.J. Yang, J.Q. Sun, D.X. Gu, P. Li, L.L. Yao, D.Y. Shi, S.N. Guo, C. Liu, Antioxidant activities of sulfated codonopsis polysaccharides in acute oxidative stress, J. Food Biochem. 45 (2021).
[64] Hossein Hassanian-Moghaddam, Rafizadeh Ali, Shariati Shahab, Rafizadeh Melika, Zamani Nasim, Evaluation of methanol content of beverages using an easy modified chromotropic acid method, Food Chem. Toxicol. 121 (2018) 11–14.